AGU PUBLICATIONS

JGR

Journal of Geophysical Research: Space Physics

RESEARCH ARTICLE

10.1002/2015JA021271

This article is a companion to *Tao et al.* [2016] doi:10.1002/2015JA021272.

Key Points:
- Temporal variations of Jupiter's northern aurora were detected using Hisaki/EXCEED
- Auroral power enhancement are accompanied by a slight far ultraviolet color ratio (CR) increase
- CR-brightness distribution and longitude dependence are consistent with other observations

Correspondence to:
C. Tao,
chihiro.tao@nict.go.jp

Citation:
Tao, C., et al. (2016), Variation of Jupiter's aurora observed by Hisaki/EXCEED: 1. Observed characteristics of the auroral electron energies compared with observations performed using HST/STIS, *J. Geophys. Res. Space Physics*, *121*, doi:10.1002/2015JA021271.

Received 30 MAR 2015
Accepted 17 APR 2016
Accepted article online 21 APR 2016

Variation of Jupiter's aurora observed by Hisaki/EXCEED: 1. Observed characteristics of the auroral electron energies compared with observations performed using HST/STIS

Chihiro Tao[1,2,3], Tomoki Kimura[4,5], Sarah V. Badman[6], Go Murakami[4], Kazuo Yoshioka[4,7], Fuminori Tsuchiya[8], Nicolas André[1], Ichiro Yoshikawa[9], Atsushi Yamazaki[4], Daikou Shiota[10], Hiroyasu Tadokoro[11,12], and Masaki Fujimoto[4]

[1]IRAP, Université de Toulouse/UPS-OMP/CNRS, Toulouse, France, [2]Now at NICT, Tokyo, Japan, [3]Department of Geophysics, Tohoku University, Sendai, Japan, [4]ISAS, JAXA, Sagamihara, Japan, [5]Now at RIKEN, Saitama, Japan, [6]Physics Department, Lancaster University, Lancaster, UK, [7]Department of Earth and Planetary Science, University of Tokyo, Tokyo, Japan, [8]PPARC, Tohoku University, Sendai, Japan, [9]Department of Complexity Science and Engineering, University of Tokyo, Kashiwa, Japan, [10]STEL, Nagoya University, Nagoya, Japan, [11]School of Computer Science, Tokyo University of Technology, Tokyo, Japan, [12]Now at Department of Environmental Systems Sciences, Musashino University, Tokyo, Japan

Abstract Temporal variation of Jupiter's northern aurora is detected using the Extreme Ultraviolet Spectroscope for Exospheric Dynamics (EXCEED) on board JAXA's Earth-orbiting planetary space telescope Hisaki. The wavelength coverage of EXCEED includes the H_2 Lyman and Werner bands at 80–148 nm from the entire northern polar region. The prominent periodic modulation of the observed emission corresponds to the rotation of Jupiter's main auroral oval through the aperture, with additional superposed −50%–100% temporal variations. The hydrocarbon color ratio (CR) adopted for the wavelength range of EXCEED is defined as the ratio of the emission intensity in the long wavelength range of 138.5–144.8 nm to that in the short wavelength range of 126.3–130 nm. This CR varies with the planetary rotation phase. Short- (within one planetary rotation) and long-term (> one planetary rotation) enhancements of the auroral power are observed in both wavelength ranges and result in a small CR variation. The occurrence timing of the auroral power enhancement does not clearly depend on the central meridian longitude. Despite the limitations of the wavelength coverage and the large field of view of the observation, the auroral spectra and CR-brightness distribution measured using EXCEED are consistent with other observations.

1. Introduction

Aurorae represent the environment and dynamics of a coupled magnetosphere-ionosphere-thermosphere system. Jupiter's auroral emission is often categorized into three regions: low-latitude moon-footprint emission, main aurora emission, and high-latitude polar emission (see the reviews of *Clarke et al.* [2004], *Badman et al.* [2014], *Grodent* [2014], and references therein). The moon-footprint aurorae are caused by the relative motion of electrically conductive moons and plasma carried by the surrounding planetary magnetic field. The main aurora emission is associated with the plasma corotation enforcement current during the transport of the angular momentum from the planetary neutral atmosphere through the ionosphere to the magnetosphere [e.g., *Hill*, 2001; *Cowley and Bunce*, 2001; *Cowley et al.*, 2007]. Jupiter's polar region, enclosed by the main aurora, corresponds to both open and closed magnetic field lines [e.g., *Vogt et al.*, 2011]. Several auroral features in the polar region have been related to magnetospheric reconnection events [e.g., *Grodent et al.*, 2004], emissions at the open-closed field line boundary [*Pallier and Prangé*, 2004], and short-term bursts at the dayside cusp [e.g., *Waite et al.*, 2001].

The ultraviolet (UV) emissions of Jupiter's aurora are radiated from atmospheric molecular (H_2) and atomic hydrogen (H) excited by precipitating electrons. Jupiter's UV emission spectra show significant absorption by hydrocarbons [e.g., *Yung et al.*, 1982]. This absorption effect is measured as the color ratio (CR), which is defined as the ratio of the intensity of the wavelength bands unabsorbed by hydrocarbons to that of the absorbed wavelength bands. The CR represents the column density of hydrocarbons above auroral emissions because the hydrocarbons are located in the deep atmosphere. Assuming it to be related to the penetration depth of auroral electrons, the CR is used to estimate the electron energy, while the altitude profile of the hydrocarbons also modifies the CR [e.g., *Livengood and Moos*, 1990; *Livengood et al.*, 1993; *Gérard et al.*, 2003]. The auroral spectra observed using the Hubble Space Telescope (HST) Space Telescope Imaging Spectrograph (STIS) revealed that the CR varies between spatial structures [*Gustin et al.*, 2002, 2004; *Gérard et al.*, 2014] and shows short-term variations over a few tens of seconds [*Gérard et al.*, 2003]. The high-latitude emissions sometimes show electron energies and energy fluxes similar to those of the main oval emissions; however, high electron energies (large CR) with low fluxes are also present [*Gustin et al.*, 2004]. The CR related to the brightness of H Lyman α and H_2 has also been applied [e.g., *Harris et al.*, 1996], which is suggested to be sensitive to lower energy electrons because the CR refers to hydrogen atoms at a higher altitude [*Tao et al.*, 2014].

Continuous observations reveal several timescales of auroral variations. The auroral area visible to an observer needs to be accounted for when considering variations of the integrated auroral intensity [e.g., *Prangé et al.*, 2001; *Pryor et al.*, 2005] and far UV (FUV) CR [*Livengood and Moos*, 1990]. *Prangé et al.* [2001] reported a dominant intensity variation over 5–10 days associated with magnetospheric fluctuations in addition to small variations over a few hours and a longer ($>$ 6 weeks) trend. A sporadic large intensity enhancement during one planetary rotation was detected by Cassini [*Pryor et al.*, 2005]. Auroral monitoring using the HST reveals some auroral intensity enhancements when a solar wind compression region foreshock was estimated to arrive at Jupiter, while no clear correlations with reverse shocks occurred [*Clarke et al.*, 2009]. Different auroral responses to solar wind variations were observed in sets of HST observations separated by several months [*Nichols et al.*, 2009]. The timescale of the auroral intensity variation in the polar region is as short as a few tens of seconds, which is considered to reflect the localized solar wind variation. The short-term auroral bursts at the dayside cusp are found when the solar wind dynamic pressure is enhanced [*Waite et al.*, 2001]. The periodic intensity variation with a timescale of 2–3 min is suggested to be related to the pulsed magnetic reconnections at the dayside by analogy with similar phenomena observed on Earth [*Bonfond et al.*, 2011].

Temporal variations and occurrence properties under various outer (i.e., solar wind) and inner (e.g., Io volcanic activity) conditions are crucial for understanding these auroral phenomena and related magnetospheric dynamics. Our new tool for monitoring the Jovian aurora is the Extreme Ultraviolet Spectroscope for Exospheric Dynamics (EXCEED) [*Yoshioka et al.*, 2013; *Yoshikawa et al.*, 2014; *Yamazaki et al.*, 2014] on board Japan Aerospace eXploration Agency's (JAXA's) Earth-orbiting planetary telescope Hisaki. EXCEED observed extreme UV (EUV) emission from Jupiter's northern polar region, which was our main interest here, and the Io plasma torus continuously over 40 min of every 106 min of the Hisaki orbit from December 2013 to April 2014. In addition, the HST observations were also carried out during the first half of January 2014. EXCEED could detect sporadic, large auroral intensity enhancement lasting less than one planetary rotation, which was associated with auroral low-latitude intensifications observed in the HST images [*Kimura et al.*, 2015]. In this study, we investigate the time variation of the CR with auroral brightness variations using the EXCEED. Because the CR-energy relationship is model dependent, this study refers to the CR instead of converting it to electron energy. The parameters obtained in this study are estimated using the auroral emission from the entire northern polar region. Spatially resolved spectra measured through the STIS on board the HST are referred to check the spatial variations, as described in section 2. EXCEED covers different spectral ranges compared to STIS, such that we define a new CR for the EXCEED spectral analysis. The observation details of EXCEED and analyzed results, including the relationship to modeled solar wind conditions, are described in section 3. Section 4 concludes this paper.

2. Spatial Variation of Aurora Detected Using HST/STIS

Following the HST spectral analysis by *Gustin et al.* [2004], we check the CR-brightness relation using the spectra measured by HST/STIS over the first 2 weeks of January 2014.

2.1. Imaging and Spectral Observations

In the HST observations program (ID: GO13035), the FUV-MAMA detector of the STIS obtained FUV images and spectra of Jupiter's northern aurora. The auroral images were obtained using a SrF2 long-pass filter to detect H_2 emission in the wavelength range of 125–170 nm with a plate scale of ~0.0224 arc sec pixel^{-1}. We used geometric distortion-corrected imaging data in "x2d" files with a unit of c/s. The long slit with a size of 52×0.5 arc sec^2 with G140L grating provides spatially resolved spectra at wavelengths of 110–170 nm with a resolution of ~1.2 nm. We used the flux- and wavelength-calibrated two-dimensional spectra in x2d files with a unit of erg s^{-1} cm^{-2} Å^{-1} arc sec^{-2}. On each HST orbit, the observations were made in the following

Table 1. Summary of the Imaging and Spectral Observations Conducted Using the STIS: Date, Start Time in UT, Corresponding CML, Brightness Over 155–162 nm, CR_{STIS}, Brightness Over 138.5–144.8 nm, and CR_{EXCEED} Derived From the STIS Spectra at the Main Aurora on the Disk, Emitted Power Over 138.5–144.8 nm, and CR_{EXCEED} Derived From the EXCEED Observation at the Timing Closest to the STIS Spectral Observation of Each Event

		STIS Image Observation 1 (Exposure 700 s)		STIS Spectral Observation (Exposure 200 s)		STIS Image Observation 2 (Exposure 736 s)		STIS Spectra Values of the Main Aurora on the Disk				EXCEED Values Closest to the STIS Spectral Observation	
#	Date 2014	Start Time (UT)	CML (deg)	Start Time (UT)	CML (deg)	Start Time (UT)	CML (deg)	Brightness (155–162 nm)[a]	CR_{STIS}	Brightness (138.5–144.8 nm)[a]	CR_{EXCEED}	Emitted Power (138.5–144.8 nm) (GW)[c]	CR_{EXCEED}
1	Jan 1	03:02	173	03:23	186	03:32	191	2.4	2.0	0.60	1.1	24.	1.1
2	Jan 2	09:19	192	09:40	204	09:49	210	6.8	4.3	1.3	1.8	27.	1.6
3	Jan 3	04:27	166	04:47	178	04:57	184	9.9	2.8	2.0	1.2	19.	1.4
4	Jan 4	01:10	197	01:31	210	01:40	215	2.1	1.7	0.58	1.0	32.	1.2
5	Jan 5	05:52	158	06:12	171	06:21	176	7.9	3.2	1.5	1.3	26.	1.4
6	Jan 6	02:35	190	02:55	202	03:05	208	2.1	2.1	0.44	0.92	18.	1.1
7	Jan 7	07:16	151	07:37	163	07:46	169	9.3[b]	3.6	1.5	1.3	24.	1.6
8	Jan 10	03:48	117	04:09	129	04:18	135	–	–	–	–	22.	1.4
9	Jan 11	00:31	149	00:52	161	01:01	167	19.9	3.1	4.0	1.3	40.	1.4
10	Jan 11	19:39	122	20:00	134	20:09	140	–	–	–	–	22.	1.2
11	Jan 13	01:56	141	02:16	153	02:26	159	5.2[b]	2.6[b]	0.94[b]	1.0[b]	22.	1.5
12	Jan 13	21:03	115	21:24	127	21:33	133					19.	1.4
13	Jan 13	22:39	172	22:59	185	23:09	191	2.9	2.1	0.62	1.1	17.	1.3
14	Jan 16	00:03	165	00:24	177	00:33	183	2.8	2.5	0.57	1.1	11.	1.1

[a]Unit is 10^{-13} mW m^{-2} arc sec^{-2}.
[b]The STIS slit only crosses the aurora at the limb.
[c]The auroral power after the background subtraction, without scaling for visibility of the auroral region.

sequence, image (700 s), spectrum (200 s), and image (736 s), using a time-tag mode, such that the exposure time could be divided into shorter integration times. We use the time-integrated spectra and images over each interval in this analysis. This sequence was repeated for 14 HST orbits spaced over 2 weeks. The intensity profiles from the filtered images were compared to the slit spectra across the full wavelength range by accounting for the filter throughput the function. The slit position in the north-south direction is determined by the position of the limb, and that in the east-west direction was determined by matching the intensity profile along the slit with the profiles from the images obtained before and after the spectral observations. The date, time, and system III central meridional longitude (CML) of the spectral and image observations used in this study are summarized in Table 1.

2.2. Results

Figure 1a shows the HST image and slit position of the spectral observation (white vertical line) obtained on the same HST orbit on 2 January 2014. The slit crosses from the top to the bottom, the main auroral oval at the limb, faintly enhanced high-latitude emission, and the main auroral oval on the disk. These three regions are seen in the spatial profile of the auroral brightness along the slit (Figure 1b, left), as shown by light blue, red, and blue lines, respectively. Figures 1c and 1d show the image and profile obtained on 7 January in the same format. The emission intensity of the main aurora on 7 January was lower except for localized enhancement around noon at the limb. The high-latitude emission is faint in the region under the slit (Figure 1d). The localized bright high-latitude emission is detected in the auroral image (Figure 1c). The typical FUV CR used for the STIS spectra is defined as the intensity ratio between the wavelength bands unabsorbed by the hydrocarbons $I_{(155–162\ \mathrm{nm})}$ and the wavelength bands absorbed by the hydrocarbons $I_{(123–130\ \mathrm{nm})}$, i.e.,

$$\mathrm{CR_{STIS}} = I_{(155–162\ \mathrm{nm})}/I_{(123–130\ \mathrm{nm})}\ , \quad (1)$$

where I is the height-integrated intensity of the emission, e.g., in units of kilo-Rayleigh (kR) or photons s^{-1} integrated over the wavelength of the subscript. The absorption cross section of methane is shown using the blue line in Figure 2c. The STIS spectra are provided in energy flux units, while the CR is provided in photon flux units. A ratio of (155–162 nm)/(123–130 nm) obtained from the original STIS spectra is multiplied by 1.25 to account for the unit change. For simplicity, the viewing angle is not considered in our procedure; i.e., $\mathrm{CR_{STIS}}$ is derived using the emission in each pixel. The $\mathrm{CR_{STIS}}$ values 2 and 8 are related to electron mean energies of 60 keV and 170 keV, respectively, for an eddy diffusion coefficient of $1.4 \times 10^6\ \mathrm{cm^2\ s^{-1}}$ at the homopause (see *Gérard et al*. [2003] for details). The $\mathrm{CR_{STIS}}$ profiles along the slit (Figures 1b (right) and 1d (right)) vary up to ~6, with larger values in the high-latitude region and the main oval on the disk. The time variations of the emitted power at these wavelengths and $\mathrm{CR_{STIS}}$ for the entire HST campaign are shown in Figure 1e and Table 1. The intensities are integrated over 200 s. The signal-to-noise ratio is high as indicated by the short error bars. The relationship between the unabsorbed brightness at wavelengths of 155–162 nm and $\mathrm{CR_{STIS}}$ varies between the spatial regions (Figure 1f). $\mathrm{CR_{STIS}}$ increases with the emitted power at the main auroral oval (light blue pluses and blue crosses). $\mathrm{CR_{STIS}}$ in the high-latitude region (red diamonds) has two components: one component is similar to the main aurora and the other component shows a lower intensity and higher $\mathrm{CR_{STIS}}$.

This relationship is comparable with the relationship between the electron energy and electron energy flux derived by *Gustin et al*. [2004]. Their main auroral oval and high-latitude regions correspond to the main aurora at the disk and high-latitude emission here, respectively. The regional $\mathrm{CR_{STIS}}$-brightness relation obtained here is consistent with their results from a different data set. The $\mathrm{CR_{STIS}}$ at the limb takes small values, as also observed by *Gustin et al.* [2002] and *Gérard et al*. [2014].

3. Temporal Variation of the Aurora Detected Using Hisaki/EXCEED

3.1. Observations

EXCEED counts EUV photons as a function of the position along the slit and wavelength dispersion. We used the data set obtained using the dumbbell-shaped slit, which detected emissions from the Io plasma torus and Jupiter's northern polar region simultaneously. The slit shapes and a sample imaging spectrum are shown in Figures 2a and 2b, respectively. The slit width in the polar region is 20 arc sec in the north-south direction (along Jupiter's rotation axis) with an effective spatial resolution along the slit (dawn-dusk direction) of 17 arc sec [*Yoshikawa et al*., 2014] and a pointing accuracy of ±2 arc sec. The red solid lines in Figure 1a show

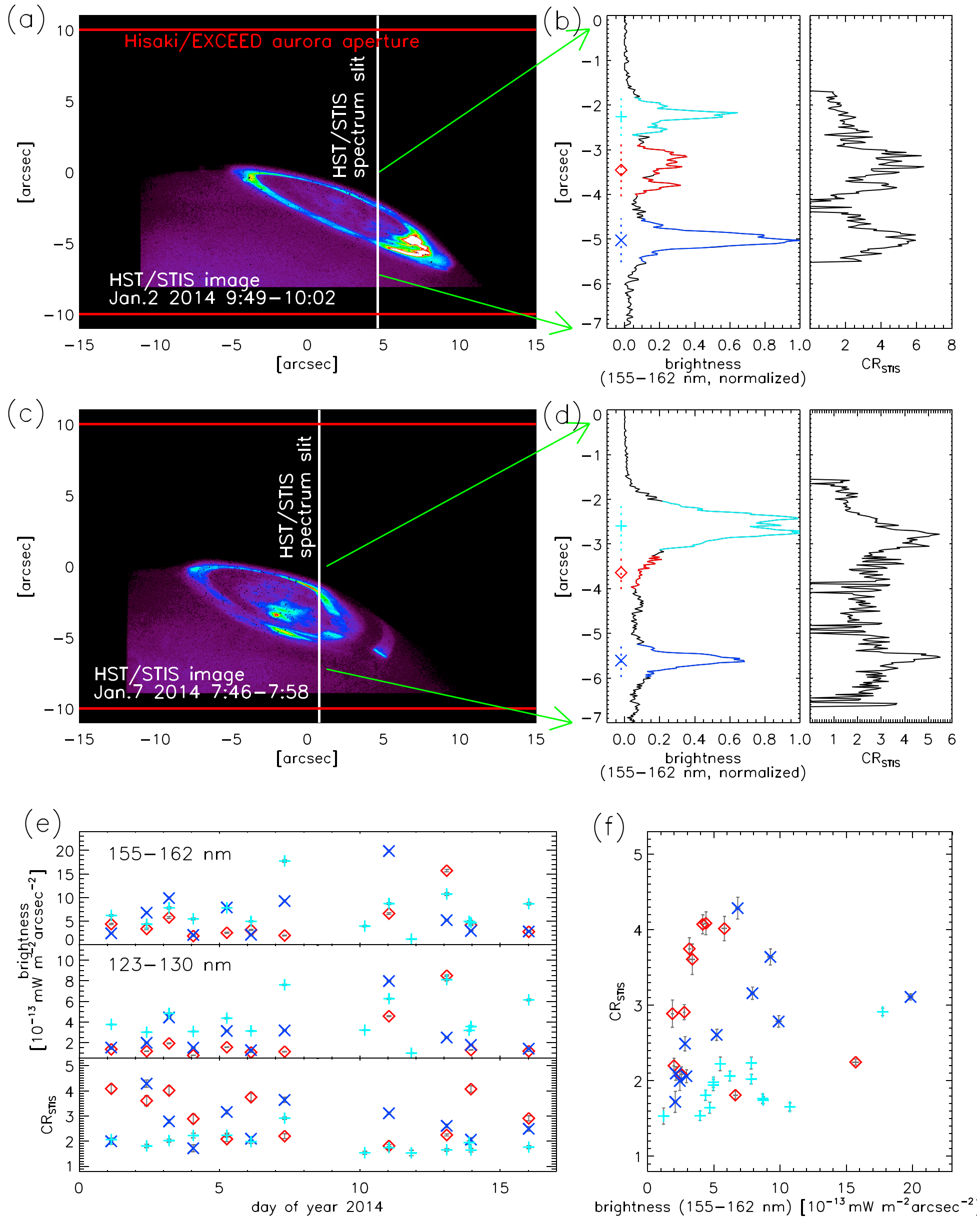

Figure 1. (a) Image of Jupiter's northern polar region, (b) the spatial profiles of the observed brightness integrated over wavelengths of (left) 155–162 nm and the (right) CR from the spectral observation along the slit on 2 January 2014, (c) the image and (d) the spatial profiles of the brightness and CR observed on 7 January 2014, (e) the time variations of the auroral brightness emitted at wavelengths (top) of 155–162 nm and (middle) of 123–130 nm and (bottom) the time variation of the CR, and (f) the relationship between the brightness at wavelengths 155–162 nm and the color ratio. The values in Figures 1e and 1f are taken at the main auroral oval on the disk (blue crosses), main auroral oval at the limb (light blue pluses), and high-latitude polar region (red diamonds) along the spectral slit, with error bars (grey lines). The corresponding auroral structures are shown using the same colors in Figures 1b (left) and 1d (left) for 2 and 7 January, respectively. Figures 1a and 1c are shown in the same linear color scale. The aurora aperture of EXCEED is bounded by the two red lines in Figures 1a and 1c, and white vertical lines show the positions of the STIS slit for the spectral observations.

the coverage of the EXCEED auroral aperture in the northern hemisphere. The data set excluded times when Jupiter was eclipsed by the Earth or Hisaki was located in the southern Atlantic anomaly. Under the latter, the instruments were turned off to avoid effects of energetic particles precipitated from the terrestrial radiation belts. Here we analyze the data obtained from 21 December 2013 to 31 January 2014 when the EXCEED time coverage was maximum. EXCEED detects auroral emission in the wavelength range of 80–148 nm, covering

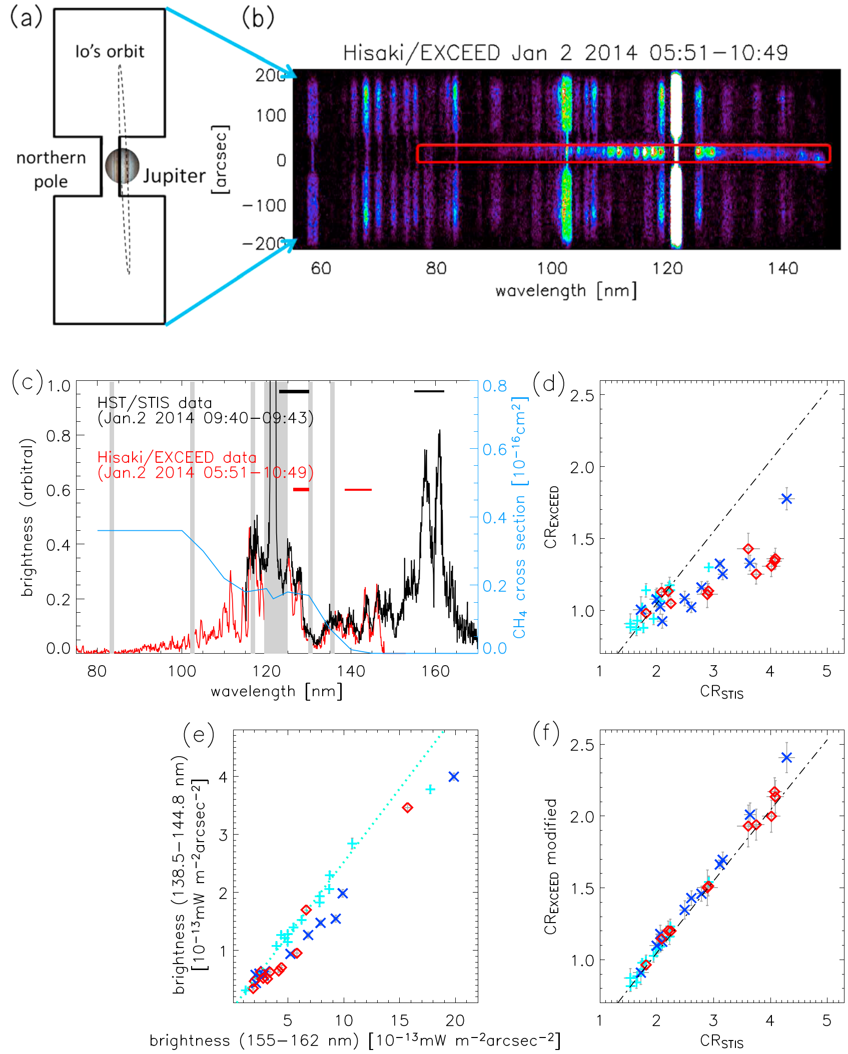

Figure 2. (a) Schematics of the observation geometry of EXCEED using the dumbbell-shaped slit, (b) imaging spectrum measured by EXCEED, (c) auroral spectra measured on 2 January by STIS integrated over the slit (black) and by EXCEED over the full polar region (red), and the relationships (d) between the two color ratios, CR_{STIS} and CR_{EXCEED}, determined from the STIS spectra (e) between the brightness at the wavelength bands less affected by absorption selected for the STIS (155–162 nm) and EXCEED (138.5–144.8 nm) and (f) between CR_{STIS} and modified CR_{EXCEED}, estimated using STIS spectra. The values for the main auroral oval (blue crosses), main auroral oval at the limb (light blue pluses), and high-latitude region (red diamonds) with error bars (grey lines) were derived. In Figure 2c, the grey hatched regions correspond to the H Lyman, He, and O emission lines from geocorona. The absorption cross section for methane [*Parkinson et al.*, 2006] is indicated by the blue line corresponding to the right-hand axis, and the two wavelength bands used for the CR estimations are shown using the horizontal lines. The dash-dotted line in Figures 2d and 2f shows the reference relation between CR_{STIS} and CR_{EXCEED} based on the CH_4 absorption effect. The light blue dotted line in Figure 2e is the best fit to the brightness values obtained for the main aurora at the limb.

part of the H_2 Lyman (B→X) and Werner (C→X) band emissions with a full width at half maximum resolution of 0.3 nm. We convert the photon counts arriving at the EXCEED detector into the photon flux at each wavelength referring to the effective area [*Yoshikawa et al.*, 2014]. Then, the number flux is converted into energy flux and integrated over a half hemisphere assuming isotropic emission to derive the total emitted power. Figure 2c shows the spectra measured using STIS (black line) and EXCEED (red line) close in time. Except for the geocoronal emission range (e.g., around 121.6 nm Lyman α) and spectral edges, the spectra observed using EXCEED and STIS are consistent. The data are integrated over certain wavelength bands (described in section 3.2) and over 10 min to improve the signal-to-noise ratio, such that the variations in the northern auroral activity over timescales from a few tens of minutes to a few months are detected. The long temporal coverage of the average auroral activity provided by the EXCEED data set is complementary to the short temporal (approximately seconds) and spatial variations observed with STIS [e.g., *Gérard et al.*, 2003; *Gustin et al.*, 2004; *Gérard et al.*, 2014] (section 2.2).

3.2. CR for EXCEED

EXCEED covers a wavelength range up to 148 nm, such that the CR_{STIS} given by equation (1) is not directly applicable. An alternate CR_{EXCEED} is defined as

$$CR_{EXCEED} = I_{(138.5\text{–}144.8\ \mathrm{nm})}/I_{(126.3\text{–}130\ \mathrm{nm})}. \tag{2}$$

We selected these two wavelength ranges for CR_{EXCEED} using the following criteria: (i) the CH_4 absorption cross section is significantly different in the two wavelength ranges; (ii) H_2 self-absorption is not effective at these wavelengths, i.e., >120 nm [e.g., *Gustin et al.*, 2013]; and (iii) EXCEED has good sensitivity. A factor of (144.8 + 138.5)/(130 + 126.3) = 1.10 is multiplied to the ratio of the intensities in power units for EXCEED, as for CR_{STIS} in section 2.2.

We used the 14 STIS spectral observations to determine the relationship between CR_{STIS} and CR_{EXCEED}. For each observation, a spectrum from the main oval (blue crosses), high-latitude (red diamonds), and limb auroral (light blue pluses) regions was obtained and used to derive the two CRs (Figure 2d). The expected ideal relation of CR_{STIS} and CR_{EXCEED} represented by the dash-dotted line is based on the CH_4 absorption cross section (see Appendix A for details). The derived values follow the ideal relation in the small CR range (CR_{STIS} <2.5, CR_{EXCEED} <1.2) as expected; however, departures from the ideal relation increase at larger CR. Although the absorption by methane is dominant, acetylene (C_2H_2) and ethane (C_2H_6), which have a significant absorption cross section up to 145 nm, should also affect our estimations of the CR. The brightness derived from the less-absorbed wavelength bands selected for the STIS (155–162 nm) and EXCEED (138.5–144.8 nm) show two linear relations (Figure 2e). The brightness from the main aurora around the limb (light blue pluses) shows one linear relation with a slope of approximately 0.26 (light blue dotted line), and the brightness in the other regions (blue crosses and red diamonds) also show linearity with a shallower slope. The former would be largely contributed by high-altitude emission, which is less affected by the hydrocarbon absorption. For the disk emission subject to absorption, H_2 emission at wavelengths of 138.5–144.8 nm is attenuated more than that at 155–162 nm by hydrocarbons. Because this attenuation decreases CR_{EXCEED} through its numerator, CR_{EXCEED} increases less rapidly than CR_{STIS}. When CR_{STIS} increases (>3), the absorption at 138.5–144.8 nm becomes more important because the ethane optical depth becomes significant. We obtain the modified CR_{EXCEED} using the brightness in the wavelength range of 138.5–144.8 nm replaced by the expected linear relation (the dotted line in Figure 2e) referring to the unattenuated band of CR_{STIS}. In this modified estimation, the relation between CR_{STIS} and the modified CR_{EXCEED} closely follows the expected relation (shown in Figure 2f). Because EXCEED integrates over various regions with weak and strong hydrocarbon absorption, the application of this conversion factor is not simple, such that we do not apply this modification in this and a companion paper [*Tao et al.*, 2016]. This analysis also highlights the possible discrepancy in the brightness and CR_{EXCEED} caused by this wavelength band selection and the observing geometry. Owing to the monotonic relation of the CRs, the aforementioned modification does not qualitatively affect the main results of this as well as the companion papers.

Here we briefly estimate the CR_{EXCEED} variations comparable with the previous observations. The measurements of CR_{STIS} at the main oval vary between 1.5 and 5 and can reach ~10 [*Gustin et al.*, 2002, 2004]. In the CR defined by *Livengood and Moos* [1990], $CR = I_{(155.7\text{–}161.9\ \mathrm{nm})}/I_{(123\text{–}130\ \mathrm{nm})} \times (1300\text{–}1230)/(1619\text{–}1557)$, wavelength ranges close to those used to define CR_{STIS} are used. They applied this result to earlier International Ultraviolet Explore (IUE) observations to find CR variations mainly in the range of 1–5, sometimes increasing up to ~8. According to the ideal CR_{STIS}–CR_{EXCEED} relation, a variation between the values of 0.7–2 with a maximum of ~5 is expected.

3.3. Spatial Integration Effect of the EXCEED Observations

We check (1) the effect of spatial integration along the slit on the derived emitted powers and CR using the STIS spectral data set and (2) a hypothesis that a large CR and a small brightness derived from the EXCEED data can also represent a relative enhancement of the high-latitude emission. We derive the CR_{EXCEED}-

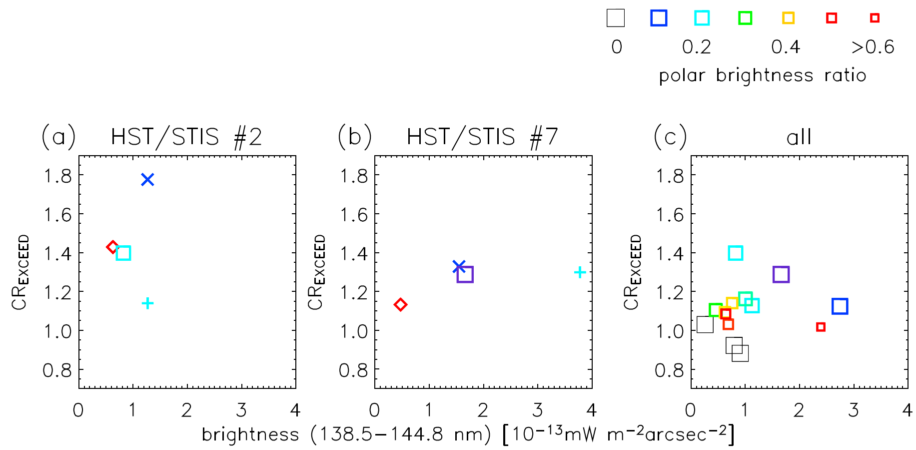

Figure 3. Relationships between the auroral emitted power at wavelengths of 155–162 nm and the CR using the similar format as Figure 1f for observations (a) on 2 January 2014 and (b) on 7 January 2014. The squares indicate the values estimated from the observation integrated over the entire auroral region along the slit in each observation, and those for (c) all events are shown. The color and size of the squares represent the ratio of the brightness of the high-latitude region to the total auroral brightness integrated along the slit according to the legend at the top.

brightness relation from the auroral brightness spatially averaged over the entire auroral region under the STIS slit, shown by the squares in Figure 3. The relation derived from the observations performed on 2 January (event #2) are located almost centrally between the CR_{EXCEED}-brightness relations of different auroral components, i.e., the main aurora (blue cross), high-latitude emission (red diamond), and main aurora at the limb (light blue plus), as shown in Figure 3a. The ratio of the high-latitude brightness to the brightness integrated along the slit is 0.24 for this event. A similar distribution is seen from the observation on 7 January (event #7), with a smaller high-latitude-to-total brightness ratio of 0.14 owing to the faint high-latitude feature captured under the slit (Figure 3b). Therefore, the CR_{EXCEED}-brightness relations derived from the auroral brightness integrated over the full auroral region are intermediate between the values determined for different spatial regions. This can be representative of the EXCEED field of view over the entire northern auroral region as described in the following sections. Figure 3c shows the spatially integrated CR_{EXCEED}-brightness relations, color coded according to the polar brightness ratio, for all cases. Relatively large polar brightness events (>0.4) are seen with small average brightness, $(0.4–1.2) \times 10^{-13}$ mW m^{-2} arc sec^{-2}, and CR_{EXCEED} ~1–1.2. The only exceptional event with a high brightness of ~2.4×10^{-12} mW m^{-2} arc sec^{-2} and CR_{EXCEED} of ~1 is observed on 13 January. In addition, events with a smaller polar brightness ratio of ~0.2 are also seen at similar brightness-CR_{EXCEED} values. Therefore, this data set cannot establish the spatially resolved analysis.

3.4. Temporal Variations of the EXCEED Observations

Figure 4 shows the time variations of the auroral emitted power observed with EXCEED from 21 December 2013 (day of year 2014, DOY −10) to 31 January 2014 (DOY 31). The power emitted at wavelengths of 138.5–144.8 nm (Figure 4a) and 126.3–130 nm (Figure 4b) varies over several timescales. Over the timescale of one planetary rotation, the emitted power at 138.5–144.8 nm changes from ~10 to ~40 GW. The upper limit of the observed emitted power varies more than the lower limit, i.e., ~20 GW at DOY 15, ~40 GW at DOY 0–10, and ~60 GW at DOY ~20 and DOY −7. In addition, two different types of enhancement can be seen. The first type is short-term, occurring within one planetary rotation, on DOYs 4, 11, and 14, as reported by *Kimura et al*. [2015] (the periods shown in orange color in Figures 4a–4f). The other type of enhancement is long term (lasting several planetary rotations, the periods shown in light blue color) at DOY −10 to −6, DOY 1–2, and DOY 17–27. The power emitted at 126.3–130 nm also varies similarly.

The power emitted at wavelengths of 138.5–144.8 nm has a clear CML dependence, as shown in Figure 5a. The dashed red line shows the length of the dayside auroral oval on the visible disk as a function of the CML. This length is obtained from the region in the northern ionosphere mapping to an *L* value of 30 using the VIP4 magnetic field model plus the ring current contribution [*Connerney et al*., 1998, Table 4]. The red solid line shows this scaled profile with a constant added to match the magnitude of the observed emitted

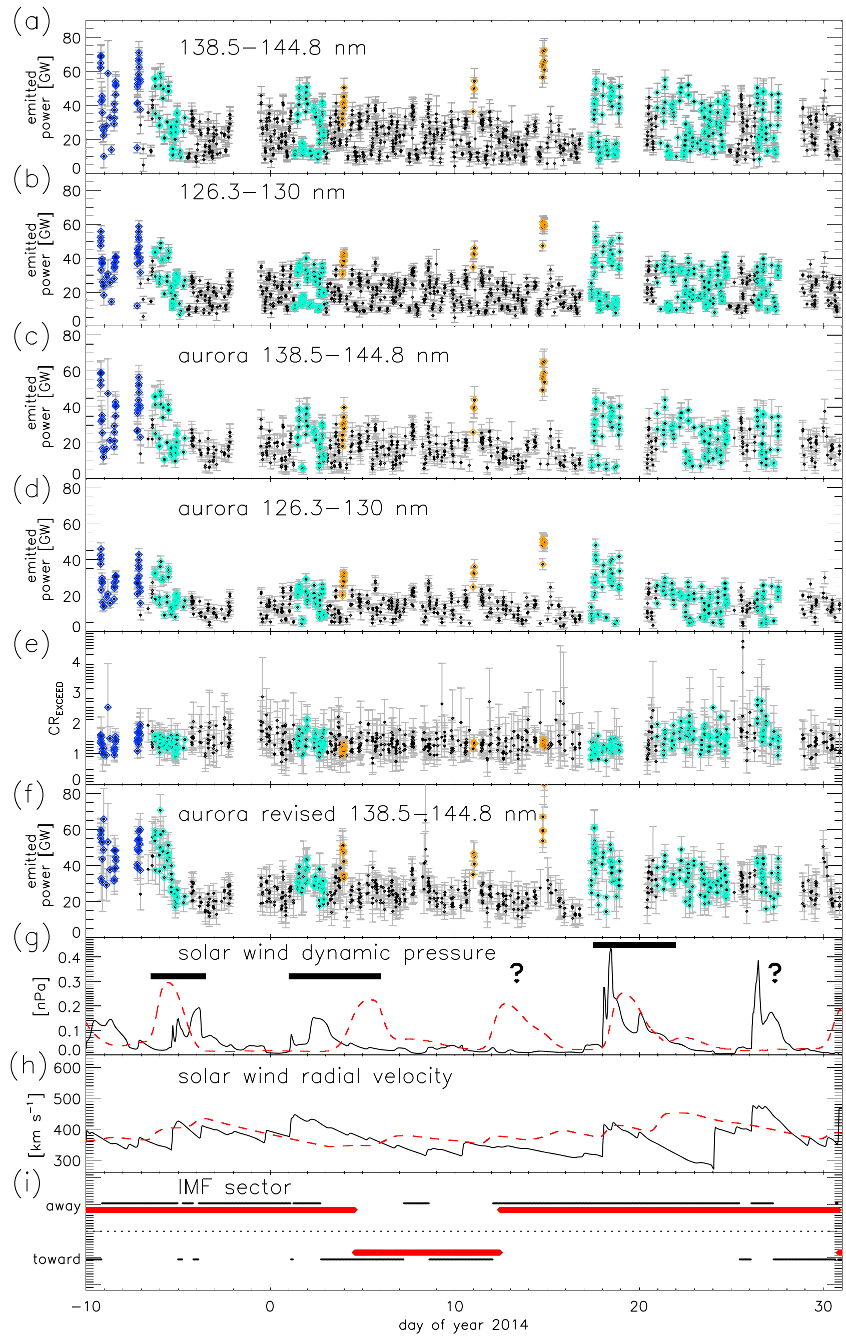

Figure 4. Time variations of the total power emitted at wavelengths (a) of 138.5–144.8 nm and (b) 126.3–130 nm; (c, d) those from aurora (with background subtraction, see the text); (e) CR, observed with EXCEED (black points) with error bars representing photon statistics errors (grey lines); (f) the emitted power scaled for visibility of the auroral region; and time variations of the solar wind (g) dynamic pressure, (h) radial velocity, and (i) the IMF sector, estimated using a 1-D model (black lines) and SUSANOO (thick or dashed red lines). The periods of short-term and long-term auroral emitted power enhancements are shown in orange and light-blue colors, respectively, except for the intermittent observation before DOY 7 as shown in blue. The solar wind dynamic pressure enhancements observed in both the 1-D and SUSANOO models are shown using the horizontal thick bars in Figure 4g.

power profile. The average of the emitted power in 36 CML bins is shown using the green lines. Their profile in CML is comparable with that of the scaled visible auroral area (red solid line). The EXCEED observation includes emission from the entire region including those inside and outside the auroral oval, which adds variations in the CML dependence. According to the observation of Jupiter's auroral emission performed using

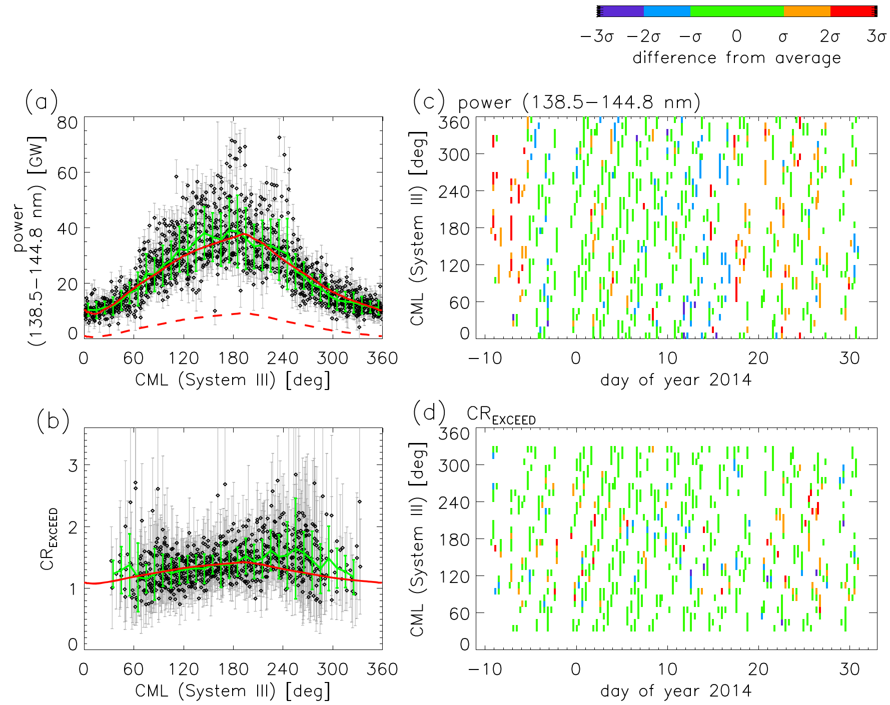

Figure 5. (a) Power emitted at wavelengths of 138.5–144.8 nm and (b) CR_{EXCEED} shown as a function of the system III CML over DOYs from −11 to 31 2014, and the color maps of (c) the power emitted at wavelengths of 138.5–144.8 nm and (d) CR_{EXCEED} normalized by standard deviations σ in 36 CML bins (as in color bars), as functions of the time and the CML. In Figures 5a and 5b, the black dots are observed points and the grey lines show their errors, and the average values in 36 CML bins are shown using the green lines with error bars representing the standard deviation. The red solid lines in Figures 5a and 5b are the fits to the average of each parameter using the relative northern auroral area shown by the red dashed line in Figure 5a.

the Cassini/Ultraviolet Imaging Spectrograph at 111.5–191.2 nm, the background disk emission can be small compared to the auroral emission in the wavelength range covered by EXCEED below 148 nm [*Pryor et al.*, 2005]. Airglow emission and aurora at the limb can affect the derived emitted power in addition to the background disk emissions, as seen by the nonzero emitted power detected at a CML of ~0° when the aurorae are on the antiobserver/nightside of the planet. In order to minimize these effects, the auroral emitted powers are derived by subtracting a 5 day running average of the emitted powers measured when $0° < \mathrm{CML} < 30°$. The subtracted power (7–15 GW) is smaller than the auroral dynamic variation (15–80 GW).

The revised auroral emitted power at wavelengths of 138.5–144.8 nm is shown in Figure 4c, and that at 126.3–130 nm is shown in Figure 4d. CR_{EXCEED} is derived as the ratio of the background-subtracted emitted powers, and large signal-to-noise (>1.5) data are used. Figure 4e shows the observed CR_{EXCEED} during this period is in the range of 0.8–2 and sometimes enhances to ~4.5, which is comparable with the previous observations described in section 3.2. The values of CR_{EXCEED} during the short- or long-term auroral enhancements are similar to those before and after the events, except for the CR_{EXCEED} enhancement after DOY 20. Figure 4f shows the auroral emitted power at wavelengths of 138.5–144.8 nm scaled for visibility of the auroral region by multiplying the factor (maximum visible auroral length at all CMLs)/(visible auroral length at instantaneous CML). A short-term enhancement on DOY 8 becomes visible in addition to the three other short-term events. Long-term variations are similar to those described above with modified amplitudes.

3.5. Solar Wind Model and Comparison With Aurora

We compare the auroral variation with solar wind parameters predicted using different models. A one-dimensional (1-D) magnetohydrodynamic (MHD) model propagates the observed solar wind conditions around Earth to Jupiter [*Tao et al.*, 2005]. For the model input, we use OMNI 1 h data, which are calibrated solar wind archive based on solar wind observations around the Earth (e.g., http://omniweb.gsfc.nasa.gov/html/ow_data.html). During the observations from 21 December 2013 to 31 January 2014 of interest here, Jupiter was located at opposition on 6 January and the Earth-Sun-Jupiter angle was small enough ($<30°$) to estimate the arrival time of solar wind pressure enhancement with a good accuracy of ~1 day [*Tao et al*., 2005]. The weakness of the 1-D model is the treatment of the longitudinal variation, e.g., localized disturbance related to coronal mass ejections, which pass either Jupiter or Earth. We confirm that the longitudinal-limited structures are not probable during the investigated term before mid-January referring to 3-D models of ENLIL [e.g., *Odstrcil and Pizzo*, 1999] and SUSANOO [*Shiota et al*., 2014]. We also refer to a 3-D model. SUSANOO solves 3-D MHD propagation of the solar wind parameters from the vicinity of the Sun based on synoptic maps of the photospheric magnetic field provided by the Global Oscillation Network Group (GONG) and empirical models. Good accuracy in predicting the interplanetary magnetic field (IMF) sectors using the 3-D model is evaluated at the positions of planets (see details in *Shiota et al*. [2014]). A difference in the predicted arrival time of solar wind at Jupiter of ±1 day can be brought by an ambiguity of $\pm 20\,\mathrm{km\,s^{-1}}$ if the propagation velocity is $400\,\mathrm{km\,s^{-1}}$, while 3-D MHD models also provide at least this ambiguity so far.

Large enhancements in dynamic pressure (>0.1 nPa) lasting a few days on DOYs ~ -6, 1–4, and 17–21 are predicted by both the 1-D and 3-D SUSANOO models with less than 2 day difference in the arrival time between the two models (Figure 4g). A pressure enhancement on DOYs 12–14 is only predicted with the 3-D model, while that on DOY 26–28 is only found using the 1-D model. The enhanced pressure events obtained in both models are close to the auroral brightness enhancement lasting longer than one planetary rotation (light blue color in Figure 4). The short-term (less than one planetary rotation) enhancements of the auroral brightness have a shorter duration than the solar wind pressure variation. The auroral response to the solar wind pressure enhancement on DOY 26–28 is not clear, which would be partly due to the continued auroral enhancement after DOY 17. The cross-correlation coefficients between the auroral revised power averaged over 0.2 day and the solar wind model show a weak correlation with maximum correlation coefficients of 0.28 for the 1-D model and 0.35 for the 3-D model with a 1 day lag, despite the ambiguity of the solar wind models. The solar wind radial velocity is small ($<500\,\mathrm{km\,s^{-1}}$, Figure 4h) in both models. The CR shows a less clear dependence on the solar wind parameters. The IMF sector is mainly "away," i.e., directed outward from the Sun, before DOY ~3 and after DOY12, and becomes "toward" to the Sun at other times (Figure 4i). From the 1-D model, the sector is judged from the azimuthal component of the IMF. The IMF sectors estimated using the 1-D model are consistent with those obtained using the 3-D model (Figure 4i).

3.6. CML Dependence

The CML dependence of the auroral emission was examined in previous studies [e.g., *Livengood and Moos*, 1990]. We analyze it using the EXCEED data to evaluate its stability and to find whether the EXCEED parameters are consistent with it. The power emitted at wavelengths of 138.5–144.8 nm has a clear CML dependence reflecting the fraction of the aurora visible to an observer as seen in section 3.3 and Figure 5a. The $\mathrm{CR_{EXCEED}}$ with large signal-to-noise ratio (>1.5) is shown as a function of CML in Figure 5b. Both the power and CR vary with the CML. The emitted power maximizes at CML of ~170°. This is a bit lower than that the CML at which the visible auroral area maximizes. The $\mathrm{CR_{EXCEED}}$ maximizes at a slightly higher CML of ~260°. The average and variance σ of these parameters in each CML bin are shown using the green line and its error bar, respectively. Because the variance of the emitted power is large enough compared to its errors (grey lines in Figure 4a), the deviation from the average behavior is significant. On the other hand, the error is large and comparable to the variance σ for the $\mathrm{CR_{EXCEED}}$ case for several points.

Next, we show the temporal variation of the CML dependence of the emitted power (Figure 5c) and $\mathrm{CR_{EXCEED}}$ (Figure 5d). The differences from the average values in each CML bin are shown using the color maps, where the white parts indicate no available data. It is difficult to find specific CML dependences of the auroral brightness enhanced events in this dataset. For example, a short-term enhancement occurs at CMLs of 120°–180° on DOY 11 (small enhancement by ~σ), and at CMLs of 150°–250° on DOY 14 (large enhancement by $> 2\sigma$). Long-term events, e.g., until DOY-5, DOY 1–2, and DOY 17–27, show enhancements over large CML ranges. The enhancement of the flux ratio by $>\sigma$ above the averaged profile also does not show a clear CML dependence.

The CML offsets of the peak emitted power and CR values from the auroral visibility profile exhibit the same trends as reported by *Livengood and Moos* [1990], i.e., the peak emitted power at a lower CML and the peak

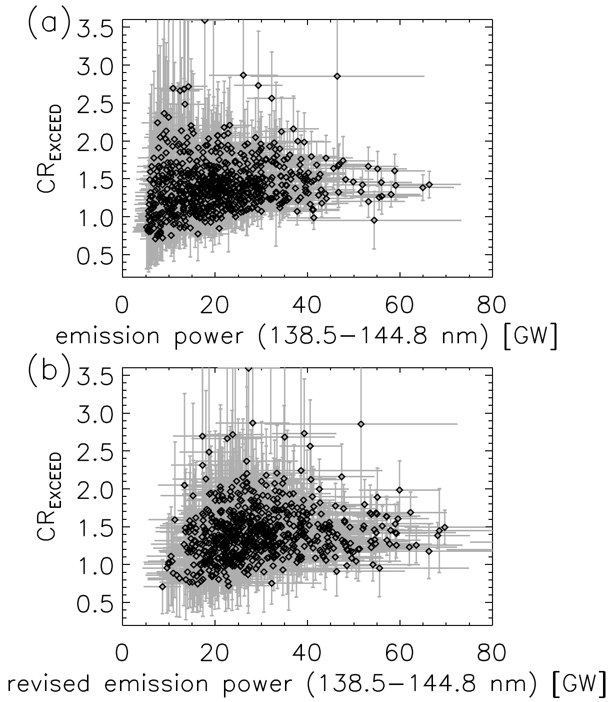

Figure 6. (a) Relationship between the power emitted at wavelengths of 138.5–144.8 nm and CR_{EXCEED} and (b) relationship between the scaled emitted power (scaled for visibility of the auroral region) and CR_{EXCEED}. The observed relations are shown using the black points.

CR at a higher CML. An enhancement of the CR in the dawnside region (~8 h magnetic local time) was reported using the spatially resolved HST spectral analysis by *Gustin et al*. [2004]. The distorted northern main auroral oval provides a better view of the dawnside at CMLs larger than ~200°, which might cause the shift in the CML of the peak CR.

3.7. CR-Brightness Relations From the EXCEED Observations

The CR-power relations from the EXCEED observations are shown in Figure 6a. Because the high-latitude-integrated power varies with the CML owing to the auroral aperture, we change the power by multiplying by the factor (the maximum visible auroral length in the all CML)/(the visible auroral length at instantaneous CMLs). The CR-power relation is modified as shown in Figure 6b. The distribution in the auroral emitted power and CR_{EXCEED} map exhibits a triangular envelope. The lower edge is at CR_{EXCEED} = ~0.7–1.5 with the emitted power increase from ~10 to 70 GW. The upper edge of the envelope increases linearly with the emitted power from ~8 to 25 GW, reaching a maximum CR_{EXCEED} of ~3. At a power greater than 25 GW, the upper edge of the envelope decreases, seeming to approach CR_{EXCEED} of ~1.4 for the greatest emitted power. This behavior suggests that the large emitted power events are mainly caused by primary particles with low average energies that are not significantly attenuated by the hydrocarbons. A few points with lower CR_{EXCEED} values appear at the lowest power values and others outside the triangular concentration have large uncertainties. This is comparable with the STIS results (Figure 1f) with less scatter because of the spatial integration (Figure 3c and section 3.3).

4. Conclusions

Auroral spectra with a good time resolution (~10 min) and a long coverage of over ~40 days obtained using Hisaki/EXCEED provide a unique opportunity to investigate the temporal variation of Jupiter's auroral parameters. The brightness-CR relation obtained from the EXCEED observations is compared with that obtained from the spatially resolved STIS observations. The main results from the observations from the end of 2013 to January 2014 are summarized as follows.

1. The EXCEED results are consistent with the STIS and previous observations in their auroral spectral profile, CML dependence, and CR-brightness distribution despite the limitation of the different wavelength coverage and large field of view of EXCEED.
2. The enhancement of the auroral brightness by a factor of 2–5 over short-duration (< one planetary rotation) and long-duration (> one planetary rotation) intervals are observed at both wavelength bands that are absorbed and unabsorbed by hydrocarbons. Therefore, compared to the brightness variation, the CR is relatively constant during this enhancement. Because the temporal variations of the solar wind dynamic pressure are different between the 1-D and 3-D models, decisive assessments of correlations between the aurora and solar wind parameters cannot be made. This study still suggests that the long-term large enhancement of the auroral power could be correlated with the large solar wind dynamic pressure enhancement. Further statistical survey is planned as future work.

3. The variability of the integrated auroral emitted power over the polar region is mainly attributed to the rotation of Jupiter's main auroral oval with the planet. The auroral CR also varies with a low dependence on the planetary rotation phase. A clear CML dependence of either short- or long-term auroral emitted power enhancements is not identified from the averaged CML data.

The quantitative estimation of the auroral parameters and further exploration of electron origin are described in the companion paper [*Tao et al.*, 2016]. The EXCEED observations and these findings cover spatially integrated auroral features and therefore represent the activity of the auroral region as a whole. Localized auroral features should exist, as shown by previous auroral observations [e.g., *Gérard et al*., 2014], which will be one of the targets of upcoming Juno observations. In addition, examination of these characteristics is also planned using the next EXCEED Jupiter observing season, from the end of 2014 to early 2015 and beyond. Comparison with direct solar wind monitoring by Juno during its cruising phase is also expected.

Appendix A

The relation between color ratios CR_{EXCEED} and CR_{STIS}, which are referring to different wavelength ranges, are represented by the hydrocarbon absorption cross sections [*Gustin et al*., 2002]. The observed spectral intensity including absorption by dominant absorber CH_4 can be expressed in terms of absorption cross section σ of CH_4, CH_4 column density N_{CH4}, and unabsorbed height-integrated spectrum intensity I' as

$$I_{(138.5-144.8\ \mathrm{nm})} = I'_{(138.5-144.8\ \mathrm{nm})} \exp\left(-N_{CH4}\,\sigma_{(138.5-144.8\ \mathrm{nm})}\right) . \tag{A1}$$

Using this and similar relations for other wavelength ranges, we obtain the following expressions for the CRs as

$$\begin{aligned} CR_{STIS} &= I_{(155-162\ \mathrm{nm})}/I_{(123-130\ \mathrm{nm})} \\ &= I'_{(155-162\ \mathrm{nm})}/I'_{(123-130\ \mathrm{nm})} \exp\left\{-N_{CH4}\left(\sigma_{(155-162\ \mathrm{nm})} - \sigma_{(123-130\ \mathrm{nm})}\right)\right\}, \end{aligned} \tag{A2}$$

$$\begin{aligned} CR_{EXCEED} &= I_{(138.5-144.8\ \mathrm{nm})}/I_{(126.3-130\ \mathrm{nm})} \\ &= I'_{(138.5-144.8\ \mathrm{nm})}/I'_{(126.3-130\ \mathrm{nm})} \exp\left\{-N_{CH4}\left(\sigma_{(138.5-144.8\ \mathrm{nm})} - \sigma_{(126.3-130\ \mathrm{nm})}\right)\right\}. \end{aligned} \tag{A3}$$

Substituting N_{CH4} obtained from equation (A2) into equation (A3),

$$CR_{EXCEED} = I'_{(138.5-144.8\ \mathrm{nm})}/I'_{(126.3-130\ \mathrm{nm})} \times \left\{CR_{STIS}\, I'_{(123-130\ \mathrm{nm})}/I'_{(155-162\ \mathrm{nm})}\right\}^{\beta} \tag{A4}$$

$$\beta \equiv \left(\sigma_{(138.5-144.8\ \mathrm{nm})} - \sigma_{(126.3-130\ \mathrm{nm})}\right)/\left(\sigma_{(155-162\ \mathrm{nm})} - \sigma_{(123-130\ \mathrm{nm})}\right), \tag{A5}$$

where $I'_{(155-162\ \mathrm{nm})}/I'_{(123-130\ \mathrm{nm})} = 1.1$ [e.g., *Grodent et al*., 2001; *Gérard et al*., 2014], $I'_{(138.5-144.8\ \mathrm{nm})}/I'_{(126.3-130\ \mathrm{nm})} = 0.59$ (estimated using the STIS spectra), and $\sigma_{(126.3-130\ \mathrm{nm})} = 1.73\times10^{-17}\ \mathrm{cm}^2$, $\sigma_{(138.5-144.8\ \mathrm{nm})} = 5.70\times10^{-19}\ \mathrm{cm}^2$, $\sigma_{(123-130\ \mathrm{nm})} = 1.74\times10^{-17}\ \mathrm{cm}^2$, and $\sigma_{(155-162\ \mathrm{nm})} = 5.33\times10^{-24}\ \mathrm{cm}^2$ are derived from *Parkinson et al*. [2006].

Acknowledgments
We acknowledge the working teams of Hisaki/EXCEED, WIND, ACE, and OMNI. This work is also based on observations made using the NASA/ESA Hubble Space Telescope (observation ID: GO13035), obtained at the Space Telescope Science Institute (STScI), which is operated by AURA, Inc. for NASA. HST data are available from STScI. The data of the Hisaki spacecraft are in the Data Archives and Transmission System (DARTS) of JAXA. ENLIL simulation results were provided by the Community Coordinated Modeling Center at the Goddard Space Flight Center through their public runs on request system (http://ccmc.gsfc.nasa.gov). The CCMC is a multiagency partnership between NASA, AFMC, AFOSR, AFRL, AFWA, NOAA, NSF, and ONR. The ENLIL model was developed by D. Odstrcil at the University of Colorado Boulder. The OMNI data used for the 1-D solar wind model are taken from the NASA Coordinated Data Analysis Web (CAWeb). This research was partly supported by a Grant-in-Aid for scientific research from the Japan Society for the Promotion of Science (JSPS, 15 K17769). S.V.B. was supported by the Royal Astronomical Society Research Fellowship. We thank the referees for their productive and valuable comments.

References

Badman, S. V., G. Branduardi-Raymont, M. Galand, S. Hess, N. Krupp, L. Lamy, H. Melin, and C. Tao (2014), Auroral processes at the giant planets: Energy deposition, emission mechanisms, morphology and spectra, *Space Sci. Rev*., doi:10.1007/s11214-014-0042-x.

Bonfond, B., M. F. Vogt, J.-C. Gérard, D. Grodent, A. Radioti, and V. Coumans (2011), Quasi-periodic polar flares at Jupiter: A signature of pulsed dayside reconnections?, *Geophys. Res. Lett*., *38*, L02104, doi:10.1029/2010GL045981.

Clarke, J. T., D. Grodent, S. Cowley, E. Bunce, P. Zarka, J. Connerney, and T. Satoh (2004), Jupiter's aurora, in *Jupiter: The Planet, Satellites and Magnetosphere*, edited by F. Bagenal, B. McKinnon, and T. Dowling, pp. 639–670, Cambridge Univ. Press, Cambridge, U. K.

Clarke, J. T., et al. (2009), Response of Jupiter's and Saturn's auroral activity to the solar wind, *J. Geophys. Res*., *114*, A05210, doi:10.1029/2008JA013694.

Connerney, J. E. P., M. H. Acuña, N. F. Ness, and T. Satoh (1998), New models of Jupiter's magnetic field constrained by the Io flux tube footprint, *J. Geophys. Res*., *103*, 11,929–11,939, doi:10.1029/97JA03726.

Cowley, S. W. H., and E. J. Bunce (2001), Origin of the main auroral oval in Jupiter's coupled magnetosphere-ionosphere system, *Planet. Space Sci*., *49*, 1067–1088.

Cowley, S. W. H., J. D. Nichols, and D. J. Andrews (2007), Modulation of Jupiter's plasma flow, polar currents, and auroral precipitation by solar wind-induced compressions and expansions of the magnetosphere: A simple theoretical model, *Ann. Geophys*., *25*, 1433–1463.

Gérard, J.-C., J. Gustin, D. Grodent, J. T. Clarke, and A. Grard (2003), Spectral observations of transient features in the FUV Jovian polar aurora, *J. Geophys. Res.*, *108*(A8), 1319, doi:10.1029/2003JA009901.

Gérard, J.-C., B. Bonfond, D. Grodent, A. Radioti, J. T. Clarke, G. R. Gladstone, J. H. Waite, D. Bisikalo, and V. I. Shematovich (2014), Mapping the electron energy in Jupiter's aurora: Hubble spectral observations, *J. Geophys. Res. Space Physics*, *119*, 9072–9088, doi:10.1002/2014JA020514.

Grodent, D. (2014), A brief review of ultraviolet auroral emissions on giant planets, *Space Sci. Rev.*, doi:10.1007/s11214-014-0052-8.

Grodent, D., J. H. Waite Jr., and J.-C. Gérard (2001), A self-consistent model of the Jovian auroral thermal structure, *J. Geophys. Res.*, *106*, 12,933–12,952, doi:10.1029/2000JA900129.

Grodent, D., J.-C. Gérard, J. T. Clarke, G. R. Gladstone, and J. H. Waite Jr. (2004), A possible auroral signature of a magnetotail reconnection process on Jupiter, *J. Geophys. Res.*, *109*, A05201, doi:10.1029/2003JA010341.

Gustin, J., D. Grodent, J.-C. Gérard, and J. T. Clarke (2002), Spatially resolved far ultraviolet spectroscopy of the Jovian aurora, *Icarus*, *157*, 91–103.

Gustin, J., J.-C. Gérard, D. Grodent, S. W. H. Cowley, J. T. Clarke, and A. Grard (2004), Energy-flux relationship in the FUV Jovian aurora deduced from HST-STIS spectral observations, *J. Geophys. Res.*, *109*, A10205, doi:10.1029/2003JA010365.

Gustin, J., et al. (2013), Effects of methane on giant planet's UV emissions and implications for the auroral characteristics, *J. Mol. Spect.*, *291*, 108–117.

Hill, T. W. (2001), The Jovian auroral oval, *J. Geophys. Res.*, *106*, 8101–8107, doi:10.1029/2000JA000302.

Harris, W., J. T. Clarke, M. A. McGrath, and G. E. Ballester (1996), Analysis of Jovian auroral H Ly-α Emission (1981–1991), *Icarus*, *124*, 350–365.

Kimura, T., et al. (2015), Transient internally driven aurora at Jupiter discovered by Hisaki and the Hubble Space Telescope, *Geophys. Res. Lett.*, *42*, 1662–1668, doi:10.1002/2015GL063272.

Livengood, T. A., and H. W. Moos (1990), Jupiter's north and south polar aurorae with IUE data, *Geophys. Res. Lett.*, *17*, 2265–2268, doi:10.1029/GL017i012p02265.

Livengood, T. A., T. Kostiuk, F. Espenak, and J. J. Goldstein (1993), Temperature and abundances in the Jovian auroral stratosphere: 1. Ethane as a probe of the millibar region, *J. Geophys. Res.*, *98*, 18,813–18,822, doi:10.1029/93JE01043.

Nichols, J. D., J. T. Clarke, J. C. Gérard, D. Grodent, and K. C. Hansen (2009), Variation of different components of Jupiter's auroral emission, *J. Geophys. Res.*, *114*, A06210, doi:10.1029/2009JA014051.

Odstrcil, D., and V. J. Pizzo (1999), Distortion of the interplanetary magnetic field by three-dimensional propagation of coronal mass ejections in a structured solar wind, *J. Geophys. Res.*, *104*, 28,225–28,239, doi:10.1029/1999JA900319.

Pallier, L., and R. Prangé (2004), Detection of the southern counterpart of the Jovian northern polar cusp: Shared properties, *Geophys. Res. Lett.*, *31*, L06701, doi:10.1029/2003GL018041.

Parkinson, C. D., J. C. McConnell, L. Ben Jaffel, A. Y.-T. Lee, Y. L. Yung, and E. Griffioen (2006), Deuterium chemistry and airglow in the Jovian thermosphere, *Icarus*, *183*, 451–470.

Prangé, R., G. Chagnon, M. G. Kivelson, T. A. Livengood, and W. Kurth (2001), Temporal monitoring of Jupiter's auroral activity with IUE during the Galileo mission. Implications for magnetospheric processes, *Planet. Space Sci.*, *49*, 405–415.

Pryor, W. R., et al. (2005), Cassini UVIS observations of Jupiter's auroral variability, *Icarus*, *178*, 312–326.

Shiota, D., R. Kataoka, Y. Miyoshi, T. Hara, C. Tao, K. Masunaga, Y. Futaana, and N. Terada (2014), Inner heliosphere MHD modeling system applicable to space weather forecasting for the other planets, *Space Weather*, *12*, 187–204, doi:10.1002/2013SW000989.

Tao, C., R. Kataoka, H. Fukunishi, Y. Takahashi, and T. Yokoyama (2005), Magnetic field variations in the Jovian magnetotail induced by solar wind dynamic pressure enhancements, *J. Geophys. Res.*, *110*, A11208, doi:10.1029/2004JA010959.

Tao, C., L. Lamy, and R. Prangé (2014), The brightness ratio of H Lyman-α/H2 bands in FUV auroral emissions: A diagnosis for the energy of precipitating electrons and associated magnetospheric acceleration processes applied to Saturn, *Geophys. Res. Lett.*, *41*, 6644–6651, doi:10.1002/2014GL061329.

Tao, C., T. Kimura, S. V. Badman, N. André, F. Tsuchiya, G. Murakami, K. Yoshioka, I. Yoshikawa, A. Yamazaki, and M. Fujimoto (2016), Variation of Jupiter's Aurora observed by Hisaki/EXCEED: 2. Estimations of auroral parameters and magnetospheric dynamics, *J. Geophys. Res. Space Physics*, *121*, doi:10.1002/2015JA021272.

Vogt, M. F., M. G. Kivelson, K. K. Khurana, R. J. Walker, B. Bonfond, D. Grodent, and A. Radioti (2011), Improved mapping of Jupiter's auroral features to magnetospheric sources, *J. Geophys. Res.*, *116*, A03220, doi:10.1029/2010JA016148.

Waite, J. H., Jr., et al. (2001), An auroral flare at Jupiter, *Nature*, *410*, 787–789, doi:10.1038/35071018.

Yamazaki, A., et al. (2014), Field-of-view guiding camera on the HISAKI (SPRINT-A) satellite, *Space Sci. Rev.*, *184*(1–4), 259–274, doi:10.1007/s11214-014-0106-y.

Yoshikawa, I., et al. (2014), Extreme ultraviolet radiation measurement for planetary atmospheres/magnetospheres from the Earth-orbiting spacecraft (Extreme Ultraviolet Spectroscope for Exospheric Dynamics: EXCEED), *Space Sci. Rev.*, *184*(1–4), 237–258, doi:10.1007/s11214-014-0077-z.

Yoshioka, K., et al. (2013), The extreme ultraviolet spectroscope for planetary science, EXCEED, *Planet. Space Sci.*, *85*, 250–260.

Yung, Y. L., G. R. Gladstone, K. M. Chang, J. M. Ajello, and S. K. Srivastava (1982), H_2 fluorescence spectrum from 1200 to 1700 A by electron impact: Laboratory study and application to Jovian aurora, *Astophys. J.*, *254*, L65–L69.